

2017-11

Investigations of Offshore breaking Wave Impacts on a large offshore Structure

Hu, Z

<http://hdl.handle.net/10026.1/9984>

10.1016/j.jfluidstructs.2017.08.005

Journal of Fluids and Structures

Elsevier BV

All content in PEARL is protected by copyright law. Author manuscripts are made available in accordance with publisher policies. Please cite only the published version using the details provided on the item record or document. In the absence of an open licence (e.g. Creative Commons), permissions for further reuse of content should be sought from the publisher or author.



Investigations of offshore breaking wave impacts on a large offshore structure

Zheng Zheng Hu^{*}, Tri Mai, Deborah Greaves, Alison Raby

School of Marine Science and Engineering Faculty of Science and Environment, University of Plymouth, Plymouth, Devon, PL4 8AA, UK



HIGHLIGHTS

- Wave impact types for a truncated wall are similar to those for a full depth wall.
- A second-order NewWave inlet boundary condition is implemented in the NWT.
- Four distinct wave impact types with the same input energy are generated.
- Numerical simulations of run up and peak pressure agree well with experiments.
- The highest force on the hull occurs under the large air pocket wave impact.
- The highest run-up at the hull occurs for the slightly-breaking wave impact.
- The highest pressure recorded at any location was due to flip-through impact.
- Different wave impact types should be considered for different design purposes.

ARTICLE INFO

Article history:

Received 22 March 2016

Received in revised form 8 August 2017

Accepted 9 August 2017

Keywords:

OpenFOAM

Focused wave groups

Breaking waves

Nonlinear $k - \epsilon$ model

Air entrainment

Impact pressure

ABSTRACT

This paper describes numerical and laboratory investigations that have been carried out to gain a better understanding of the physical processes involved in offshore breaking wave impacts on a large offshore structure. The findings are relevant to offshore and coastal structures and to identifying the extreme loads, peak pressures and maximum run-up needed for their design. A truncated wall in a wave flume is used to represent a vertical section of an FPSO (Floating Production Storage and Offloading) hull, which is a typical large offshore structure. Four types of wave impact were identified in the tests, and are referred to as slightly-breaking, flip-through, large air pocket and broken wave impacts. Physical modelling was undertaken in Plymouth University's COAST Laboratory and the open source Computational Fluid Dynamics (CFD) package-Open Field Operation and Manipulation (OpenFOAM) was adopted to study focused wave generation and wave impact on the hull. The method solves incompressible Unsteady Reynolds-averaged Navier–Stokes Equations (URANSE) using a finite volume method with two phase flows. A Volume of Fluid (VoF) interface capturing approach is used to model the free surface. A NewWave boundary condition is used to generate focused wave groups based on the first plus second-order (hereafter second-order) Stokes wave theory in the Numerical Wave Tank (NWT). By changing the focus location with respect to the wall, the wave impact type was altered in both the numerical and laboratory investigations.

The results show that for the four wave impact types tested good agreement was achieved between numerical predictions and experimental measurements of surface elevation, run up and impact force. The peak pressures predicted by the simulation are lower than the experimentally measured results due to time step constraints, although the shape of the pressure time history is very similar. Four distinct wave impact types are identified

^{*} Corresponding author.

E-mail address: zheng.hu@plymouth.ac.uk (Z.Z. Hu).

for the vertical hull section and are found to be similar in character to those observed for a full depth vertical wall. The predicted force on the hull is found to be greatest for the large air pocket impact, and the highest run-up for the slightly-breaking wave impact. The pressure records show a high degree of spatial and temporal variation though the highest pressure recorded at any location was due to flip-through. This research has shown that different characteristic wave impact types are responsible for maximum load and greatest wave run-up and so need to be considered separately for design purposes.

© 2017 The Authors. Published by Elsevier Ltd. This is an open access article under the CC BY license (<http://creativecommons.org/licenses/by/4.0/>).

1. Introduction

Large offshore structures, ships, storm surge barriers and closure dams can have vertical faces that are exposed to wave impact. Such impacts can lead to very high peak pressures and wave loads, which may lead to structural failure, and are likely to be more common as storm occurrence increases due to climate change. The importance of investigating wave loading on offshore structures and in particular the loads and run-up due to wave impact under a changing climate is being recognised to an increasing extent. For example, [Tanimoto and Takahashi \(1994\)](#) described how an extreme wave impact can displace large caissons by several metres, and design formulae for estimating the magnitude of the impulsive pressure generated by breaking waves have recently been presented by [Goda \(2000\)](#) and [Oumeraci et al. \(2001\)](#). [Guilcher et al. \(2013, 2014\)](#) used the SPH (Smoothed Particle Hydrodynamics) method to model a unidirectional breaking wave impacting a rigid wall and compared the numerical predictions with experimental results under two different scales (full scale and scale 1:6). In this paper, a truncated vertical wall is used to represent a vertical section of the hull of a fixed FPSO and investigated to provide understanding of the underlying processes characterised by four wave impact types.

For coastal structures, accurate prediction of the most severe wave loading is crucial to their design. In laboratory studies, [Bullock et al. \(2007\)](#) investigated the detailed characteristics of four different types (slightly-breaking, low-aeration, high-aeration and broken) of wave impact on a vertical and sloping wall, and found that the impacts depend on the breaker conditions. [Bredmose et al. \(2010\)](#) found that the flip-through impact can generate very large localised pressure on the wall without any hint of entrained or trapped air, and [Bredmose et al. \(2015\)](#) studied the effects of scale and aeration on two impact types (flip-through and low-aeration impacts), by physical and numerical investigation. Wave impacts are very sensitive to the wave shape just before impact. For example, an air pocket may be trapped if the wave overturns as it strikes the wall, and large quantities of air can be entrained during breaking so that a turbulent air–water mixture strikes the wall when the wave has already broken. In either process, the compressibility of the trapped or entrained air will affect the dynamics, reduce the maximum pressure due to a cushioning effect, but tend to distribute the impact pressure more widely so that the overall force on the wall may not necessarily be reduced (see [Peregrine et al., 2005](#)). The presence of air may extend the duration of peak pressure and lead to rebound that can increase the total impulse on the structure (see [Wood et al., 2000](#)).

[Dold \(1992\)](#) and [Cooker and Peregrine \(1990\)](#) investigated the wave impact problem numerically by means of fully nonlinear potential flow theory, which assumes incompressible, inviscid single phase fluid flow and has been used to model wave propagation over an elliptical mound and onto a vertical wall. This gives valuable insight into the way high pressures are generated but the model suffers from the limitation of only being applicable to non-aerated flows up to a point just after the waves overturn. [Bredmose et al. \(2010\)](#) used nonlinear potential flow to study the flip-through wave impact on a wall but the numerical computation broke down during the impact while the vertical jet was emerging. [Colicchio et al. \(2007\)](#) applied a level-set method and an SPH method to model an impact that traps a small pocket of air. [Khayyer and Gotoh \(2009\)](#) developed several modified forms of the MPS (Moving Particle Semi-implicit) method which they compared with the results of [Hattori et al. \(1994\)](#) for a flip-through wave impact. The AMAZON-SC 3D code (see [Hu et al., 2013a, b](#)) used a high resolution Godunov-type approach for spatial discretisation of the Euler and Navier–Stokes equations and employed both air and water fluid regions for 3D water impact problems. It uses an exact Riemann solver for hyperbolic conservation laws, which enables shock waves to be reproduced. Two software packages CFX and STAR CCM+ were validated against measured results for an oscillating cone at the water surface by [Westphalen et al. \(2009\)](#), in which the fully nonlinear Navier–Stokes equations were solved by a control volume Finite Element (CV-FE) and a Finite Volume (FV) method in laminar fluid flow. In this paper, the incompressible Unsteady Reynolds-averaged Navier–Stokes Equations (URANSE and hereafter RANS) in OpenFOAM (hereafter OF) are solved using a finite volume method in two phase flows and the Nonlinear $k-\epsilon$ model developed by [Brown et al. \(2014, submitted for publication\)](#) is selected for this study because the turbulence model becomes important in cases of wave breaking as considered here. A Volume of Fluid (VoF) interface capturing approach is used to model the free surface, which can handle break-up, overturning and recombination, including the flow of the surrounding air and entrainment of air pockets at the hull. In this way, consideration of effects including viscosity, aeration and turbulence may be taken into account during simulation of violent wave impact. The only drawback of the study is that hydroelasticity and the compressibility of water and air is not considered in the flow solution and the effect of this omission on the quality of the results is discussed.

The impacting waves were generated using a focused wave group technique, which enables a highly nonlinear extreme wave to be produced on demand at both a given time and location. Focused wave groups have been used for impact

experiments by [Bredmose et al. \(2010\)](#), [Peregrine et al. \(2006\)](#), [Chan and Melville \(1988\)](#), [Chan \(1994\)](#), [Guilcher et al. \(2013\)](#) and [Kimmoun et al. \(2009, 2010\)](#). It is an established method of generating a deterministic large wave event that is representative of an extreme ocean wave. The large amplitude waves are placed within a wave group with an envelope that decays rapidly to zero away from the group centre and can lead to a localised occurrence of one or more extreme waves. For studies of wave structure interaction, focused groups have the advantage of giving a highly repeatable extreme wave event with almost no pre-history of preceding waves. NewWave focusing (see [Tromans et al., 1991](#)), which represents the average shape for an extreme wave profile consistent with a random process with a specified wave spectrum, is used here. [Zang et al. \(2006\)](#) carried out experiments for a fixed ship-shaped body under interaction with a NewWave group. [Ning et al. \(2008, 2009\)](#) studied the propagation of NewWave groups of four different peak wave heights and results from physical experiments and numerical study are compared. NewWave simulations and comparison with the experiment data have been considered by [Hu et al. \(2009, 2010\)](#) using the research code AMAZON-SC and by [Westphalen et al. \(2008, 2012\)](#) using the commercial CFD codes of the STAR CCM+ and CFX. In each case the test series did not involve breaking of the waves and good agreement in free surface elevation was achieved. In this paper, the wave boundary condition is based on NewWave for representation of the extreme wave event together with second-order wave correction, developed for implementation in OpenFOAM by [Hu et al. \(2014, 2016\)](#).

This paper is organised as follows: in Section 2, the numerical method in OpenFOAM is described in brief; the physical experiments are described in Section 3; results are presented for each of the four characteristic wave impacts in Section 4; finally, conclusions and recommendations for design are given in Section 5.

2. Brief description of numerical method

Although the compressibility of air may be important in some of the impact cases presented, it should be noted that the version of OpenFOAM used here assumes incompressible fluids. The governing equations, which include continuity Eq. (1) and momentum conservation Eq. (2), are given by the Reynolds Averaged Navier–Stokes (RANS) equations as follows:

$$\frac{\partial \rho}{\partial t} + \nabla \cdot \rho \mathbf{U} = 0 \quad (1)$$

$$\frac{\partial \rho \mathbf{U}}{\partial t} + \nabla \cdot (\rho \mathbf{U} \mathbf{U}) - \nabla \cdot (\mu_{\text{eff}} \nabla \mathbf{U}) = -\nabla p - \mathbf{g} \cdot \mathbf{X} \nabla \rho + \nabla \mathbf{U} \cdot \nabla \mu_{\text{eff}} + \sigma \kappa \nabla \alpha. \quad (2)$$

In these equations, \mathbf{g} is the acceleration due to gravity; ρ is the density and p represents pressure; \mathbf{X} is the position vector; \mathbf{U} denotes the velocity vector, $\mu_{\text{eff}} = \mu + \rho \nu_{\text{turb}}$ is the effective dynamic viscosity and μ is the dynamic viscosity. ν_{turb} is the turbulent kinematic viscosity and it is given by the chosen turbulence model, for example, $\nu_{\text{turb}} = C_d k^2 / \varepsilon$ for the standard k - ε model, where k is turbulent kinetic energy, ε is turbulent eddy dissipation and $C_d = 0.09$ as recommend by [Rodi \(1980\)](#).

Consider two fluids (air and water) in a computational domain. The fluids are separated by an interface (free surface). The free surface is tracked as:

$$\frac{\partial \alpha}{\partial t} + \nabla \cdot (\mathbf{U} \alpha) = 0 \quad (3)$$

where α is the indicator function and defined as the quantity of water per unit of volume in each cell. This means that if $\alpha = 1$ the cell is full of water, if $\alpha = 0$ the cell is full of air, and in any other case it contains the interface between air and water. For example, the fluid density and the dynamic viscosity of the cell are computed as follows:

$$\begin{aligned} \rho &= \alpha \rho_{\text{water}} + (1 - \alpha) \rho_{\text{air}} \\ \mu &= \alpha \mu_{\text{water}} + (1 - \alpha) \mu_{\text{air}}. \end{aligned} \quad (4)$$

The nonlinear k - ε model used here was recommended by [Brown et al. \(2014\)](#), it relates the mean strain rate of the flow to the Reynolds stress tensor through the algebraic nonlinear Reynolds stress model. The k and ε are defined as

$$\frac{\partial k}{\partial t} + \nabla \cdot (\mathbf{U} k) = P_k - \varepsilon + \nabla \cdot [(v + \sigma_k \nu_t) \nabla k], \quad (5)$$

$$\frac{\partial \varepsilon}{\partial t} + \nabla \cdot (\mathbf{U} \varepsilon) = \frac{C_{1\varepsilon}^* P_k \varepsilon}{k} - \frac{C_{2\varepsilon} \varepsilon^2}{k} + \nabla \cdot [(v + 1/\sigma_\varepsilon \nu_t) \nabla \varepsilon], \quad (6)$$

where the coefficients of $C_{1\varepsilon}^* = 1.44$, $C_{2\varepsilon} = 1.92$, $\sigma_\varepsilon = 0.77$ and $\sigma_k = 1.0$ are used. $\nu_t = C_\mu \frac{k^2}{\varepsilon}$ is the wall function and P_k is the nonlinear stress term ([Brown et al., 2014, submitted for publication](#)).

To solve for the coupled pressure and velocity field in both fluids, the InterFoam solver PIMPLE is used; it is a combination of PISO (Pressure Implicit with Splitting of Operators) and SIMPLE (Semi-Implicit Method for pressure-Linked Equations) algorithms. Its main structure is inherited from the original PISO, but it allows equation under-relaxation to ensure the convergence of all the equations at each time step. Both algorithms are thoroughly explained in VoF applications by [Jasak \(1996\)](#). Solution of Eq. (3) has to be bounded between 0 and 1 and OpenFOAM's special solver called MULES (Multidimensional Universal Limiter for Explicit Solution) uses a limiter factor on the fluxes of the discretised divergence term to fulfil these restrictions.

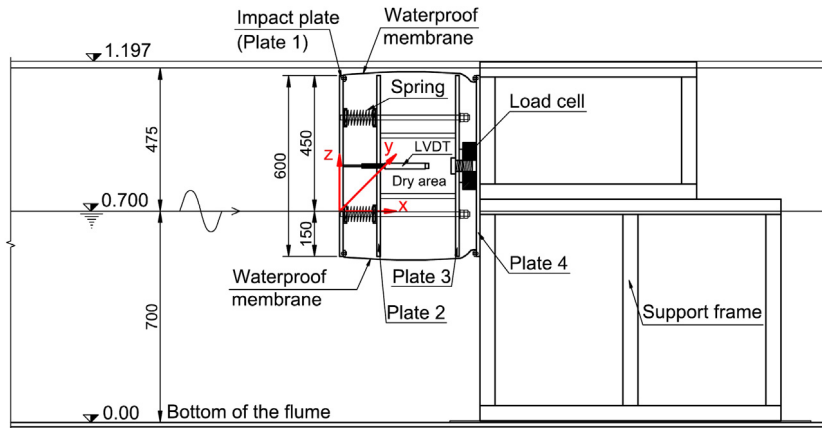


Fig. 1. Side view sketch of physical model. N.B. Springs were locked for tests reported in this paper. All dimensions in mm.



Fig. 2. Glass-walled flume showing the wave gauge and dry-backed hull section configuration.

3. Description of the experimental model

Physical modelling of extreme waves interacting with a hull section was undertaken in a glass-walled wave flume in Plymouth University's COAST Laboratory, and the setup of the experiment is shown in Figs. 1 and 2 (see Mai et al., 2015). In this paper, a Cartesian system $Oxyz$ is defined where the origin is at the right of the domain, with $x = 0$ on the face of the truncated vertical wall, on the centreline of the flume cross-section and at the Still Water Level (SWL). Orientations are defined with x pointing along the flume, y into the flume and z pointing upwards. The wave flume is 35 m long in the x direction, with a cross-section width of 0.6 m in the y direction and height of 1.2 m in the z direction, operating with a still water depth of 0.7 m. The hull section is modelled using a truncated vertical wall comprising an aluminium plate of dimensions $0.6 \text{ m} \times 0.56 \text{ m} \times 0.012 \text{ m}$ ($x \times y \times z$), connected to a rigid wall by four springs. The distance between the paddle and front impact plate is 26.9 m. Its submergence depth in the water is 0.15 m. The spring system could incorporate springs of different stiffness for an elastic hull and could also be locked to obtain a rigid hull as presented here. Pressures under wave impact were measured with FGP XPM10 pressure sensors installed at 7 locations on the vertical hull section as shown in Fig. 3. The diameter of the pressure sensor used in the experiments is 8 mm. Pressure, force and deflection data were all sampled at 35 kHz frequency to ensure the impulsive response was fully described. The force was measured by a low profile load cell as shown in Fig. 1. Tests were repeated up to 8 times to ascertain repeatability. Thirteen resistance-type wave gauges were used to measure water surface elevation along the length of wave flume with closer spacing to determine the wave profile in front of the hull. The wave gauge data were sampled at 128 Hz frequency. All test waves were focused wave groups generated using the NewWave methodology with an underlying JONSWAP spectrum ($\gamma = 3.3$). The wave was generated by application of the focused-wave group technique (see for example Baldock et al., 1996), with the focus location adjusted to produce different types of breaking wave impact. The focus distance measured from the wave paddle to the face of the truncated vertical wall was: 29.44 m for the slightly-breaking wave, 29.04 m for the flip-through wave, 28.84 m for the large air pocket wave and 28.04 m for the broken wave, respectively.

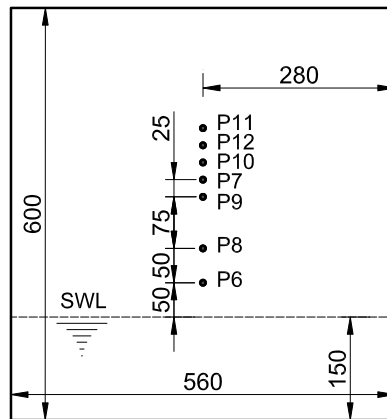


Fig. 3. Pressure sensors on the hull section. Note dimension in mm.

4. Numerical results, comparison and discussions

In the numerical simulations, water was assigned a density $\rho = 1000 \text{ kg/m}^3$ and kinematic viscosity $\nu = 10^{-6} \text{ Pa/s}$, while air density $\rho = 1.2 \text{ kg/m}^3$ and kinematic viscosity $\nu = 1.48 \times 10^{-5} \text{ Pa/s}$. Initial values are assigned of $k = 1\text{e-}8$ and $\varepsilon = 1\text{e-}11$. The volume fraction function α had a value of 0 for air and 1 for water, with $\alpha = 0.5$ representing the air–water interface. The second-order NewWave inlet boundary condition is implemented in the NWT closer to the hull than in the experiment where the wave paddle was controlled by linear wave generation. As reported previously by Hu et al. (2014), which compared first- and second-order wave generation at the inlet, the fully nonlinear numerical model agrees well with experimental measurements of the surface elevation at the focal position.

In the NWT, rather than simulating the physical motion of the wave paddle; a wave inlet boundary condition is defined in which the free surface elevation and the velocity and pressure through the water column are specified as fluxes crossing a transparent boundary. The inlet boundary condition data is based on measurements from the physical wave tank at a distance of 10.8 m from the model. The velocity and pressure data is extrapolated from the free surface elevation measurements using second order Stokes wave theory. Using this approach allows a shorter, and therefore less expensive, NWT to be used. For the NewWave input condition, expressions for the velocity components and surface elevation are based on the solution at time t calculated as described by Hu et al. (2014).

The following boundary conditions were applied. At the inlet, the velocities for the water component and surface elevation were expressed by the NewWave boundary condition for extreme waves. The velocity was specified for the water component only with the velocity of the air at the inlet boundary set to zero. The pressure was set to a zero gradient at all boundaries. The top and right far boundaries were specified with a non-reflecting boundary condition allowing air to enter or leave the domain. The remaining boundaries and the fixed structure were set as rigid walls with no-slip boundary conditions.

The wave characteristics were based on the experiment, in which the significant wave height, $H_s = 0.163 \text{ m}$, peak wave period, $T_p = 1.601 \text{ s}$ and the number of wave components, $N = 116$. For the NewWave input condition, input data included the wave amplitude of $A_i(f)$ for I component wave frequencies, $f(i)$, is used as in the experiment. The NewWave formulation and the solution procedure are described by Hu et al. (2014). In this paper, the time is based on the numerical time and a time shift is applied to the experiment data so they correspond at the focus time and position, and may be compared.

In the NWT, the geometry of the domain is defined as $13.2 \text{ m} \times 0.6 \text{ m} \times 1.3 \text{ m}$ ($x \times y \times z$). The length of the relaxation zone used to remove unwanted wave reflections at the inlet was defined to be one wavelength i.e. 4 m, and at the outlet it was applied in the region behind the wall. The water height in the NWT was $h = 0.7 \text{ m}$, matching the physical experiment, and the initial height of air above the water surface was 0.6 m. The distance between the wave inlet boundary and the front wall is 10.8 m. The vertical distribution of grid cells is chosen to be relatively coarse near the bed of the flume, but then becomes

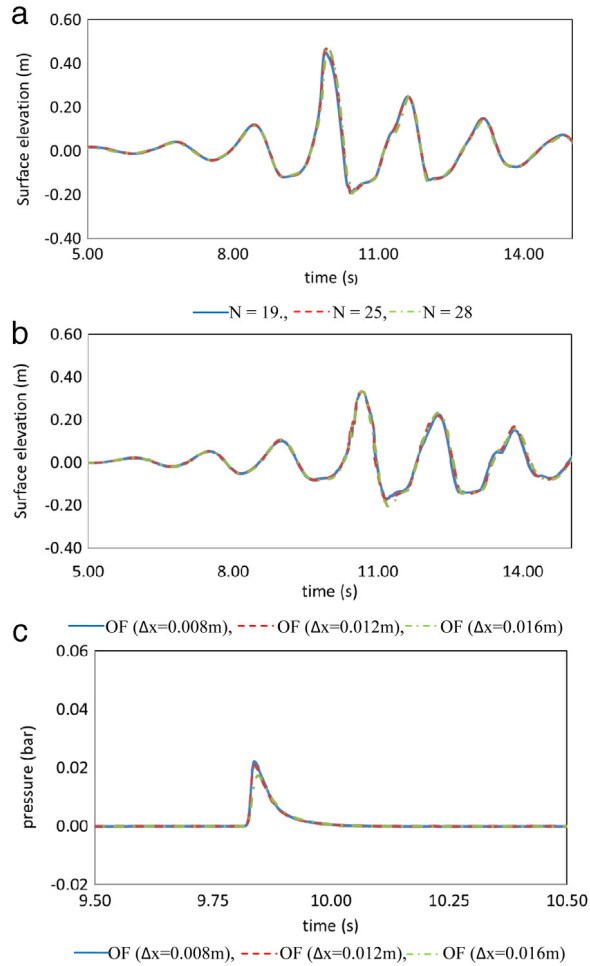


Fig. 4. (a) surface elevation at a position 0.015 m in front of the hull for numbers of wave components (b) surface elevation at a position 0.015 m in front of the hull for grid sizes in the x direction (c) pressure at p11 for grid sizes in the x direction.

finer towards the free surface. The fine region from $z = -0.21$ m to $z = 0.51$ m, which contains the hull and free surface, has a uniform mesh of $\Delta z = 0.02$ m for the cases of slightly-breaking and flip-through wave impact and a uniform mesh of $\Delta z = 0.012$ m for the cases of large air pocket and broken wave impact. Under these considerations, the NWT domain has 866,022 cells for the slightly-breaking and flip-through wave types and 1,304,794 cells for the large air pocket and broken wave types.

To investigate the potential for reducing CPU time, a numerical convergence study was carried out on the number of wave components used for the wave inlet boundary condition in the NWT. Fig. 4(a) shows the comparison of surface elevation at a position 0.015 m in front of the hull, obtained with the number of wave components, N , equal to 19, 25 and 28. From these results, it can be seen that the wave elevation obtained are almost identical for the latter two numbers, indicating that convergence was achieved using 25 wave components.

Once the number of wave components was established, mesh convergence tests were carried out using three different uniform meshes with spacings $\Delta x = 0.016$ m, 0.012 m and 0.008 m around the hull. Fig. 4(b) shows the comparison of wave elevation at a position 0.015 m to the front of the hull and the results of grid converge index of GCI_{32} is 5% and GCI_{21} is 4% (see Roache et al., 1986). Fig. 4(c) shows the comparison of pressure at P11 and the results of grid converge index of GCI_{32} is 13% and GCI_{21} is 5%. Therefore, the spacings $\Delta x = 0.0012$ m and 0.008 m are used in following numerical simulation. These confirm that the calculations are mesh convergent.

Parallel computing is used for all simulations presented in this paper, with openMPI implementation of the standard Message Passing Interface (MPI) to manage parallel distribution memory computers. A typical example of CPU running time is 1 day and 16 h using 16 cores of a High Performance Computing (HPC) cluster (a Quad core 2.56 GHz with 16 Gb), to generate a simulation time of 18 s in the slightly-breaking wave impact case. An adjustable time step is used by defining a maximum Courant number of 0.15 under a time-step of $\Delta t = 0.064$ s ($= T_p/25$) for all numerical simulations.

4.1. Characteristics of wave impact

In order to make comparisons with the physical experiments, numerical simulation of four types of wave impact were carried out by adjusting the NewWave focus location. Keeping the underlying amplitude spectra the same, but varying the focus location, allows the effect of wave shape to be investigated without changing the input wave energy. The focus time is pre-defined as $t_f = 12.80$ s ($= 8T_p$) for all four simulated wave types and the different wave impact types are characterised as follows:

- (1) Slightly-breaking impact: $x_f = 13.34$ m. This is similar to a sloshing wave impact in that its run-up is higher than its crest and the water just rises up the face of a steep wall with little loss of energy. The free surface is seen to be smooth and the wave is close to breaking (see Bullock et al., 2007).
- (2) Flip-through impact: $x_f = 13.14$ m. This wave has high steepness and an overturning wave crest that is prevented from hitting the wall by a fast-moving jet. High impact pressures are observed. According to Bredmose et al. (2010), this impact type occurs lies between sloshing and violent impact.
- (3) Large air pocket impact: $x_f = 12.94$ m. At the moment of impact the, hull section and wave enclose a large semi-circular air bubble or a dense cloud of bubbles and/or entrapped smaller air pockets (see Bullock et al., 2007).
- (4) Broken wave impact: $x_f = 11.94$ m. This wave has broken in front of the hull and produces aerated water mass that hits the hull (see Bullock et al., 2007).

Fig. 5 shows wave profiles for the four types of wave impact, the upper images are taken by video from the experiment and the lower images are snapshots of the free surface profile obtained from the numerical simulation. The different characteristics of each case can be clearly observed in these wave profiles. It is evident that the wave impact types identified for the hull section are similar to those seen at a vertical, bottom-mounted, wall. The distinctive features of each, such as wave elevation, wave pressure and wave force on the hull are discussed in more detail in the following sections.

4.2. Free surface elevations

The five wave gauges are positioned in the numerical wave tank and in the experiment at 0.015, 0.065, 0.15, 0.24 and 0.33 m measured from the front of the vertical hull. The numerical and physical results for maximum crest elevation at a position 0.015 m in front of the hull are compared in Fig. 6. The numerical prediction underestimates the measured maximum crest by 4% with a value of 0.467 m for the slightly-breaking wave, by 5% with a value of 0.448 m for the flip-through wave, by 3% with a value of 0.437 m for the large air pocket wave and by 15% with a value of 0.331 m for the broken wave. It can be seen that the maximum crest predicted for the broken wave impact has the largest difference between the numerical prediction and experimental data, likely to be due to complexities of the overturning wave, air bubbles, small aerated water mass and the compressibility of water and air.

As indicated above, the wave impacts are very sensitive to the wave shape just before impact. Comparison of the free surface profiles up to the occurrence of the four types of impact close to the hull are shown in Fig. 7, in which the good match between the numerical prediction and the experimental data may be seen. These are snapshots along the centre-line and show how the wave profile develops just before impact in each case. The plots give valuable insight into the characteristics in each wave impact. In general, the numerical prediction for the surface elevation is very close to the experimental records in these figures.

For the slightly-breaking wave, Fig. 7(a) shows the transition of the wave as it progresses towards and impacts with the hull. The numerical result shows that the wave does not overturn before hitting the hull; the water tends to rise up the hull face from approximately $t = 9.75$ s. The highest impact pressure on the hull at location P11 (see Fig. 10) occurs at $t = 9.80$ s and the maximum crest elevation of 0.527 m occurs at $t = 9.88$ s. It is noticeable that the maximum crest elevation in the numerical result is higher than the experimental value of 0.485 m because in the experiment, the wave gauge could not be positioned on the hull face, but instead is 0.015 m in front of the hull.

In the flip-through wave, Fig. 7(b) demonstrates the impact associated with no overturning and the resultant smooth flow before $t = 9.78$ s and an overturning wave crest that appears at $t = 9.82$ s. This figure demonstrates that the volume flux moving upwards from below the crest causes such a rapid rise in the water level against the hull that a vertical jet is formed at $t = 9.95$ s, which flips up through the gap in front of the approaching wave from $t = 9.91$ s. Hull and Müller (2002) also found that the vertical jet in their flip-through impact emerged as the gap between the wave front and the wall was filled by the rising water. The highest impact pressure measured on the hull at location P11 (see Fig. 10) occurs at $t = 9.91$ s while the crest and vertical jet was formed. The maximum crest elevation of 0.532 m is reached at $t = 10.05$ s. It can be seen that there is no air trapped in a flip-through impact.

For the large air pocket wave, Fig. 7(c) indicates that an overturning wave appeared at $t = 9.79$ s and water contained a large air pocket from $t = 9.93$ s to $t = 10.10$ s. In such a process, an appreciable air pocket is being trapped between the overturned wave and the hull which increases the disparity between the numerical prediction and experimental data. The highest impact pressure on the hull at location P11 (see Fig. 10) occurs at $t = 9.98$ s. There is no evidence of wave breaking before the maximum crest elevation of 0.499 m at $t = 10.10$ s, but there is evidence of a large air pocket being trapped and significant impact pressure on the hull. The air pocket or dense cloud of bubbles creates damped oscillations in both

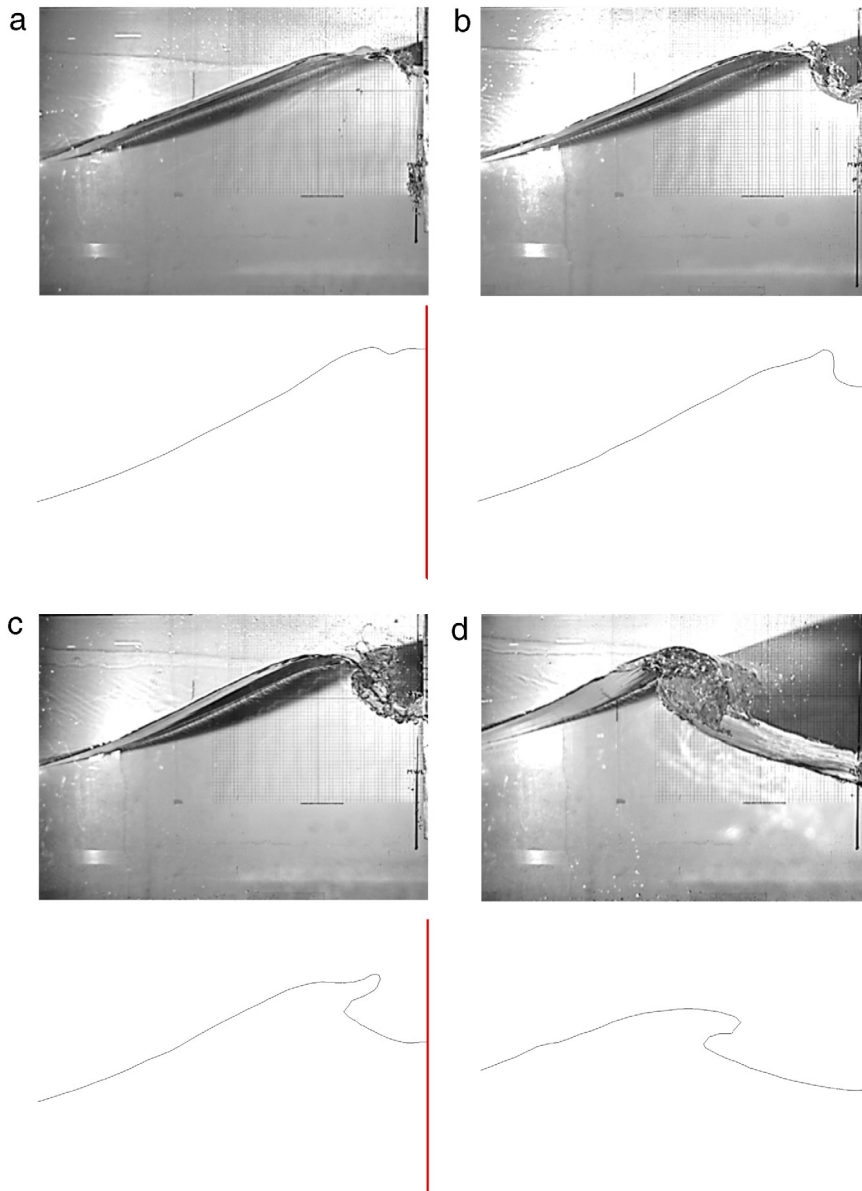


Fig. 5. Wave profiles: numerical wave profiles (upper) and wave profiles (lower) (a) slightly-breaking (b) flip-through (c) large air pocket (d) broken wave.

pressure and voids ratio, in which are evident following the time of peak pressure and are due to compression of air within the air–water mixture.

In the broken wave case, Fig. 7(d) demonstrates the impact associated with a spilling breaker that starts to break at $t = 10.32$ s. After this, the turbulence associated with the breaking process entrains significant quantities of air and a small aerated water mass forms in front of each broken wave profile as it hits the hull from $t = 10.32$ s to $t = 10.56$ s. Good agreement between the measured and predicted water surfaces is found, except for the broken wave at the locations very close to the hull ($x = -0.015$ and -0.065 m), and this may be partly due to the difficulty in measuring the surface elevation using wave gauges where the surface is disturbed and the flow is a mixture of air and water. The highest impact pressure on the hull at location P11 (see Fig. 10) occurs at $t = 10.51$ s, and the maximum crest elevation of 0.439 m arrives at $t = 10.56$ s. Unlike for the other impact types presented in which the comparison between the numerical prediction and measured free surface profiles is very good at all times during the impact, it is noticeable that there are large differences between the numerical prediction and experimental data after $t = 10.32$ s for this case. This corresponds with the time at which the breaking wave loading initiates and the entrained air undergoes alternating expansion and compression. The numerical model does not take into account compressibility effects and so cannot capture this expansion and compression.

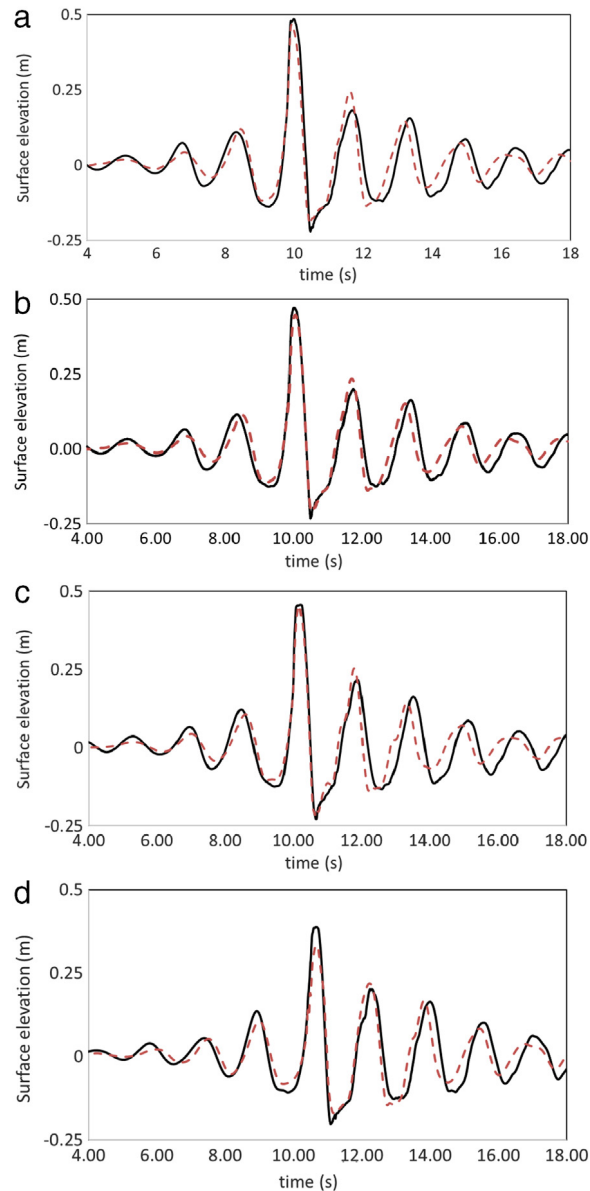


Fig. 6. Comparison of wave elevation at a position 0.015 m in front of the hull (a) slightly-breaking (b) flip-through (c) large air pocket (d) broken wave (— Phy. Exp., - - - OpenFOAM).

A numerical model that incorporates a compressible fluid model would be necessary to simulate such a broken wave impact; more information is given by [Ma et al. \(2016\)](#) and [Bredmose et al. \(2015\)](#).

4.3. Impact pressures on the hull

As is well known, the region of high pressure during wave impact is usually both temporally and spatially localised, and is extremely sensitive to geometrical factors such as wave shape and water depth. Time histories of the measured and predicted pressure at the 3 different positions, P6, P9 and P11 on the hull section (see [Fig. 3](#)) are compared for each of the four impact types in [Figs. 8–10](#) in order to identify the characteristics of each type in more detail. In each case for comparison, the experimental tests are plotted together as shown in the left hand side of [Figs. 8–10](#) and the numerical prediction is plotted together with one of those experiment data in the right hand side of [Figs. 8–10](#). The figures show that for each location and for each of the four types of wave impact, the results are generally in good agreement with experiments, although there are some differences in rise time to impact, which is partly due to the variation in the experiment for the high impact cases.

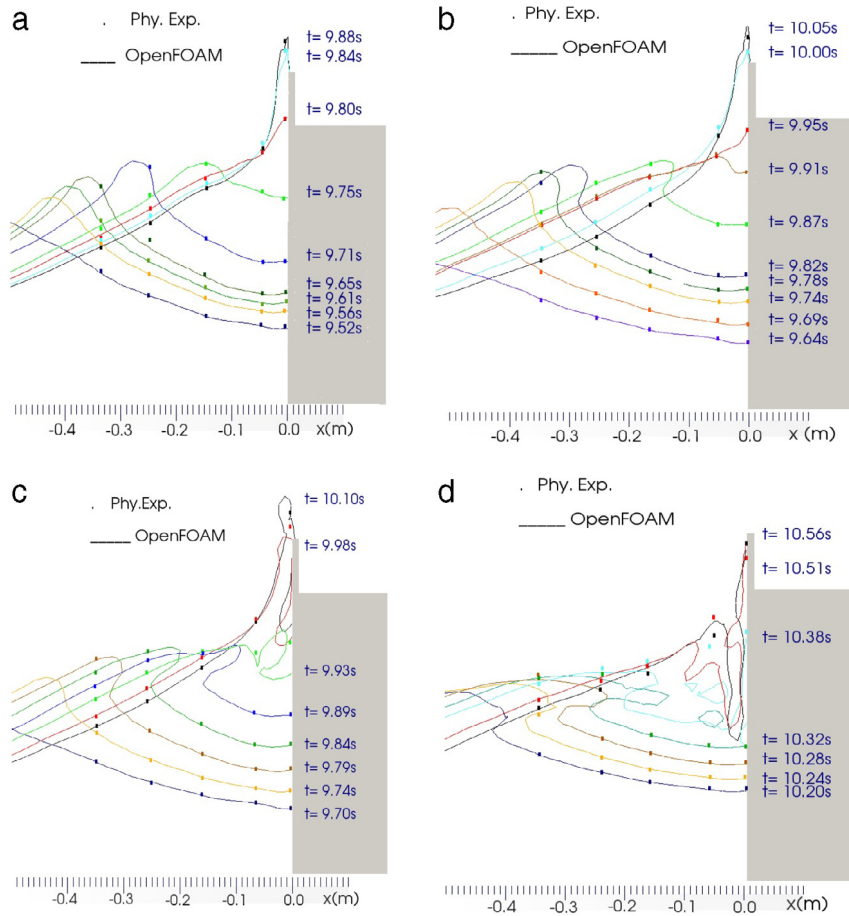


Fig. 7. Comparison of the free surface profiles close to the hull (a) slightly-breaking (b) flip-through (c) large air pocket (d) broken wave.

In the experiments, up to eight repeat tests were run for each case (see [Mai et al., 2015](#)) and the pressure data recorded at P6 and P9, located 50 mm and 175 mm above the SWL respectively, show good repeatability. For these data, a typical time history is plotted for comparison with the numerical prediction in [Figs. 8 and 9](#).

At P6 (50 mm above the SWL), shown in [Fig. 8](#), the numerical prediction of the peak pressure agrees well with the experiment. It underestimates the experiment by 5% with a value of 0.023 bar under the slightly-breaking wave impact, by 4% with a value of 0.030 bar under the flip-through wave impact, by 7% with a value of 0.040 bar under the large air pocket wave impact, and exceeds the experiment by 1% with a value of 0.026 bar under impact with the broken wave. The predictions agree reasonably well, and the different shapes of the distinctly different impact types are captured successfully. The experiment data for the flip-through and large air pocket wave impacts (see [Fig. 8\(b\)–\(c\)](#)) show pressure vibration after peak pressure has occurred, which is due to the vibration of the hull (at natural frequency of 40 Hz). The numerical result does not predict this oscillation because the hull is assumed to be rigid and hydroelasticity effects are not included.

Additional high frequency oscillations can be seen in the pressure time history for the large air pocket impact, superimposed on the structural vibrations identified above. These additional oscillations are likely to be due to the presence of a large amount of air, either entrapped as a large air pocket or entrained as a dense cloud of bubbles, and the alternate expansion and compression of this air following the time of peak pressure. The high frequency oscillations are a common feature of wave impacts with trapped air (see [Bullock et al., 2007](#)).

[Fig. 8\(d\)](#) shows the pressure time history for the broken wave impact, where the incoming wave breaks before it reaches the hull, producing a highly aerated turbulent flow. Significant quantities of air are entrained as the wave breaks and as this highly aerated water wave front hits the hull, multiple relatively low pressure spikes can be seen (see [Bullock et al., 2007](#)). The peak pressure both in numerical prediction and experiment is lower than other impacts. It can be seen that these high frequency fluctuations are superimposed on the overall pressure variation in the experimental record, which as above could have been the result of oscillation due to compressibility within irregular clouds of small bubbles (see [Bullock et al., 2007](#)).

At P9 (175 mm above the SWL), as shown in [Fig. 9](#), the numerical prediction of the peak pressure agrees well with the experiments for the first three impact types, but the difference becomes more marked for the broken wave case. The

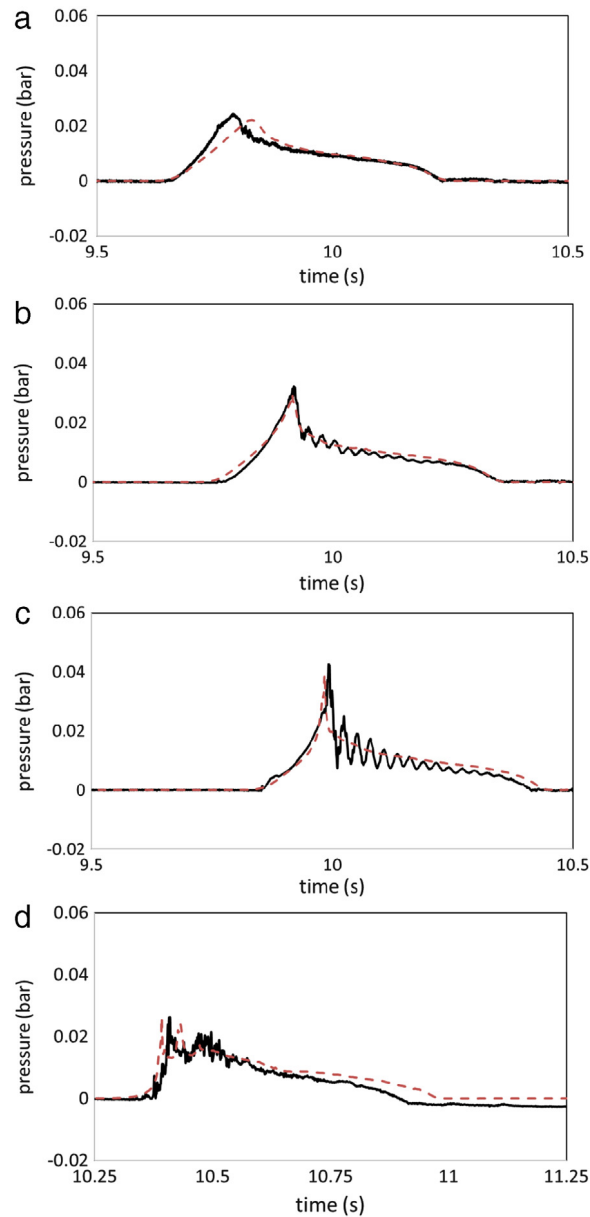


Fig. 8. Comparison of the pressure at P6 on the hull (a) slightly-breaking (b) flip-through (c) large air pocket (d) broken wave (— Phy. Exp., - - - OpenFOAM).

prediction underestimates the experiment by 3% with a value of 0.022 bar under the slightly-breaking wave impact, by 2% with a value of 0.040 bar under the flip-through wave impact, by 3% with a value of 0.068 bar under the large air pocket wave impact and overestimates the experiment by 8% with a value of 0.024 bar under impact with the broken wave. For each impact type, the rise time of the impact is shorter in comparison with that at P6. The peak pressure under the large air pocket wave impact (see Fig. 9(c)) is larger than others.

At P11 (275 mm above the SWL), the pressure time history is shown in Fig. 10. However, the data for P11, located at 275 mm above the SWL, shows considerable variability and so for each case, the all of the repeat data at P11 is plotted alongside the numerical prediction in Fig. 10. P11 is located in the splash region, the impacts are much more variable in both the shape of the pressure impact time history and the peak values. Nevertheless, in each case for p11, the prediction falls within the envelope of the experiment data. The reason for the high variability in these data is that the pressure sensor is located significantly above the SWL and in the region where splashing and multiple impacts occur. In order to capture the pressure spike correctly in the flip-through, large air pocket wave and broken wave impacts, it is necessary to use a very small time step in the numerical simulation. Here, a fixed time step of 1.0×10^{-5} is used around the time of high pressure

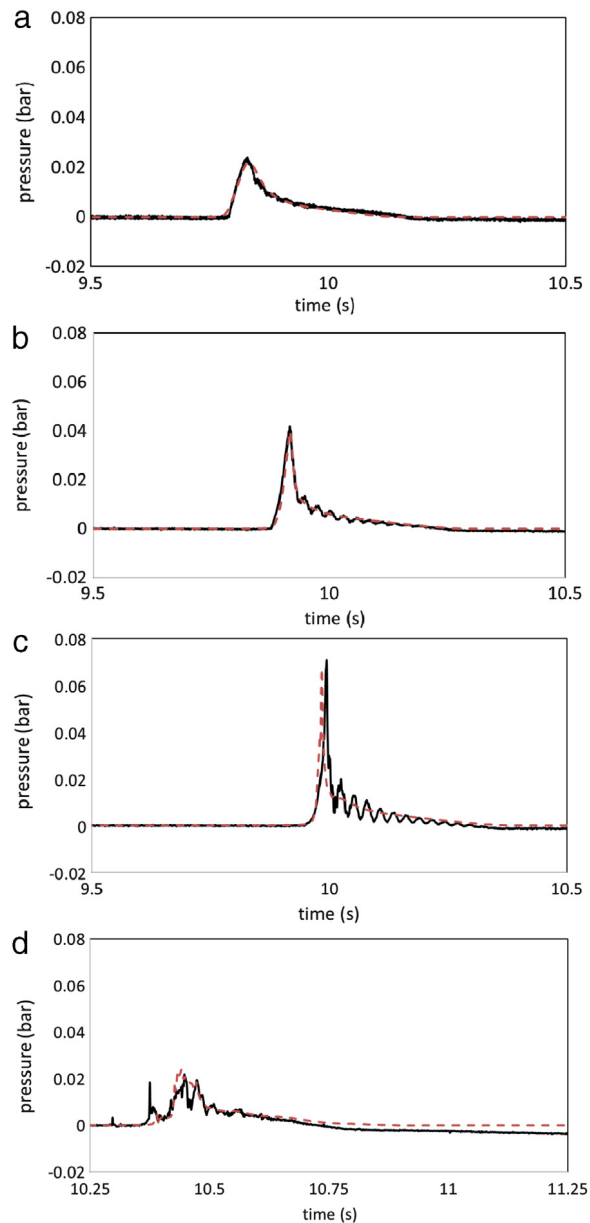


Fig. 9. Comparison of the pressure at P9 on the hull (a) slightly-breaking (b) flip-through (c) large air pocket (d) broken wave (— Phy.Exp., - - - OpenFOAM).

during the wave impacts, the experimental data were collected at 35 kHz frequency, and so the time step should be sufficient to capture the very highest pressure peaks with duration of less than a millisecond. The difference observed for flip through in Fig. 10(b) reflects the uncertainty in predicting the free surface at the highest point recorded above the waterline.

It is clear that the peak pressure under the flip-through impact is higher than the other impact types at P11 and the numerical predictions and experiments both exhibit clear characteristic differences between the impact types. The flip-through impact shows that although the flow remains smooth during flip-through, very large localised pressure on the hull is generated, as was also found for flip-through impact with a vertical wall by Bredmose et al. (2010). The time to reach peak pressure for slightly-breaking wave impact is $t = 9.80$ s, for the flip-through impact, $t = 9.91$ s, for large air pocket impact, $t = 9.98$ s and for broken wave impact is $t = 10.51$ s.

As we can see, the increase and decrease of the pressure time history is much smoother under the impact of the slightly-breaking wave in Figs. 8–10 than for other impact types as the water piles up at the hull without overturning. In the pressure traces for the flip-through and large air pocket wave impact (see Figs. 8–10(b)–(c)), appreciable sharp pressure

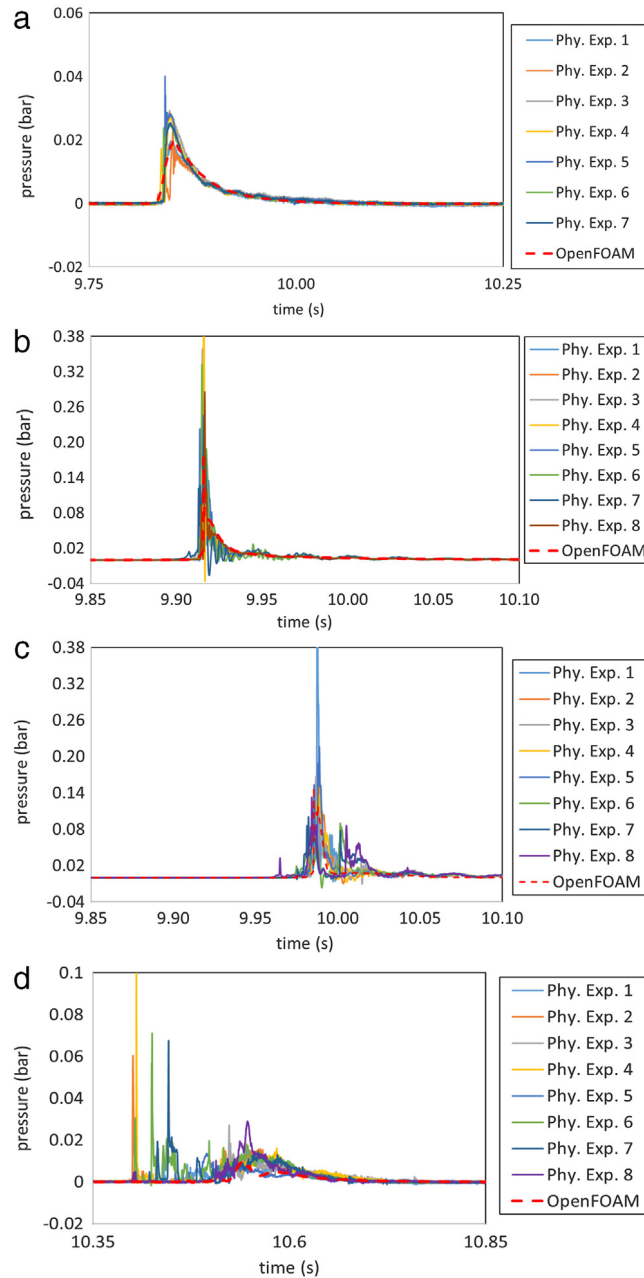


Fig. 10. Comparison of the pressure at P11 on the hull (a) slightly-breaking (b) flip-through (c) large air pocket (d) broken wave.

spikes characteristic of an impact are evident, and in these cases the wave starts to overturn just as it reaches the hull. After the sharp spike in pressure, there is a period during which the pressure oscillates at a frequency corresponding to the natural frequency of the hull section model, with a value of 40 Hz. Additional high frequency oscillation can also be seen and is due to aeration and the frequency of this is a function of the size of the air pocket. These high frequency oscillations are a characteristic of hydroelasticity and air compressibility effects and are not predicted by the numerical method used here. The impact of the broken wave (see Figs. 8–10(d)) has relatively low pressure multiple spikes that occur over a relatively longer time period as the highly aerated water forming the front of each partially broken wave hits the hull in multiple impacts and leads to pressure vibration in the air phase. It is noticeable that the peak pressures (see Figs. 8–10) are not amongst the highest reported (see Bredmose et al., 2010; Chan and Melville, 1988; Chan, 1994; Guilcher et al., 2013), although they

do provide evidence for impulsive wave impacts, and it should be noted that the set up was not optimised for traditional shallow water wave impacts.

4.4. Impact forces on the hull

The numerical prediction of horizontal force is obtained by integration of the pressure and viscous force components on the front hull section. The time histories of the force during impact are presented in Fig. 11. The time of maximum force is $t = 9.82$ s for slightly-breaking wave, $t = 9.93$ s for the flip-through wave, $t = 10.00$ s for the large air pocket wave and $t = 10.38$ s for the broken wave, respectively. It can be seen that the numerical prediction of the maximum force underestimates the experiment by 18% with a value of 0.516 kN for the slightly-breaking wave, by 38% with a value of 0.593 kN under flip-through wave, by 26% with a value of 0.899 kN under large air pocket wave impact, and by 31% with a value of 0.696 kN under the broken wave impact, respectively. The large differences in force between the prediction and experiment are likely to be due to time step and mesh size constraints and also due to the fact that the numerical prediction does not include hydroelastic effect of structural vibration. The duration of the loading is also underpredicted slightly by the numerical prediction and this may be caused by the effect of compressibility and cushioning due to the entrained air, which is not included in the incompressible numerical model, and which was observed by Peregrine et al. (2005) to elongate the force time history. As also discussed by Peregrine et al. (2005), the presence of the air pocket may spread the high pressure region across more of the hull surface and so increase the overall force. This may explain why the largest force is predicted and measured for the large air pocket case, whereas the peak pressure observed and predicted to occur for the flip-through and large air pocket wave impact are similar in size (within limitations of the measurements). Fig. 11(c) shows that the peak horizontal force under the large air pocket wave is higher and the rise time shorter than the others, which Bullock et al. (2007) also observed. The second highest peak horizontal force is under the flip-through wave impact (see Fig. 11(b)) in the experiment, although in the numerical prediction, the high force spike is not reproduced for the flip-through impact, and the broken wave case predicts a spike in the force that is not seen in experiments. However, it is clear that large air pocket and flip-through wave impacts lead to large forces and very high impact pressure and so should be given greater consideration in offshore and coastal design.

4.5. Bottom mounted wall and truncated hull

In order to assess whether the geometry of the wall has an influence on the focused wave shape before impact, the bottom mounted wall and truncated hull have been tested under the slightly-breaking wave impact and the results compared. Fig. 12 shows the surface elevation at a position 0.015 m in front of the wall and hull; the shape of the wave before impact is very similar in both cases, but the maximum surface elevation for the bottom mounted wall is larger than for the truncated hull. This is expected because in the bottom mounted case the wall blocks the entire water column, whereas in the truncated case some of the water flows under the hull. Fig. 13 shows the pressure time history at three different positions. The peak pressures (total pressure) predicted on the truncated hull are all slightly larger than on the bottom mounted wall by approximately 3% at P6, 7% at P9 and 4% at P11. This is because, although the run-up (and hence static pressure) is greater in the bottom mounted case, the dynamic pressure acting to the truncated hull is greater (see the dynamic pressure shown in Fig. 13). Fig. 14 shows the horizontal force on the wall and hull section, presented relative to the static case. The total force (F_x) on the bottom mounted wall is much larger than on the truncated hull. The reason is because the surface elevation on the bottom mounted wall is higher and because the fluid pressure is acting over a larger surface area in this case.

5. Conclusions

This study has carried out numerical and experimental investigations of wave impact on a large FPSO vertical hull section, which is modelled in the flume using a truncated vertical wall. In this work, NewWave focused groups are used to generate four distinct wave impact types of the same input energy by adjusting the focus location. The characteristic wave impact types found here for a vertical hull section (or truncated wall) are similar to those observed for a full depth vertical wall and may be categorised as: slightly breaking, flip-through, large air pocket and broken wave. This approach allows the generation of an extreme wave without significant preceding impact and is recommended as a means to model design impacts on large ocean engineering structures.

Good agreement between the numerical predictions and experimental measurements of water surface elevation as the wave approaches and runs up the hull is found and validates the numerical simulation, at least in its ability to capture the relevant phenomena. The numerical simulations presented here bring additional insights that may not be possible with the experiment measurements. For example, the largest run-up is predicted for the flip-through wave rather than as measured in the experiment for the slightly-breaking wave. The reason for the difference is that the wave elevation in the NWT may be recorded very close to the hull surface, closer than may be easily measured in the experiment.

The peak pressures predicted by the simulation are generally smaller than the experimental results due to time step constraints, but the shape of the pressure time history is very similar. The pressure records show a high degree of spatial and temporal variation, and that the highest pressure recorded at any location was due to flip-through. However, forces predicted and measured are in reasonable agreement for all impact types, and the highest force both predicted and measured on the

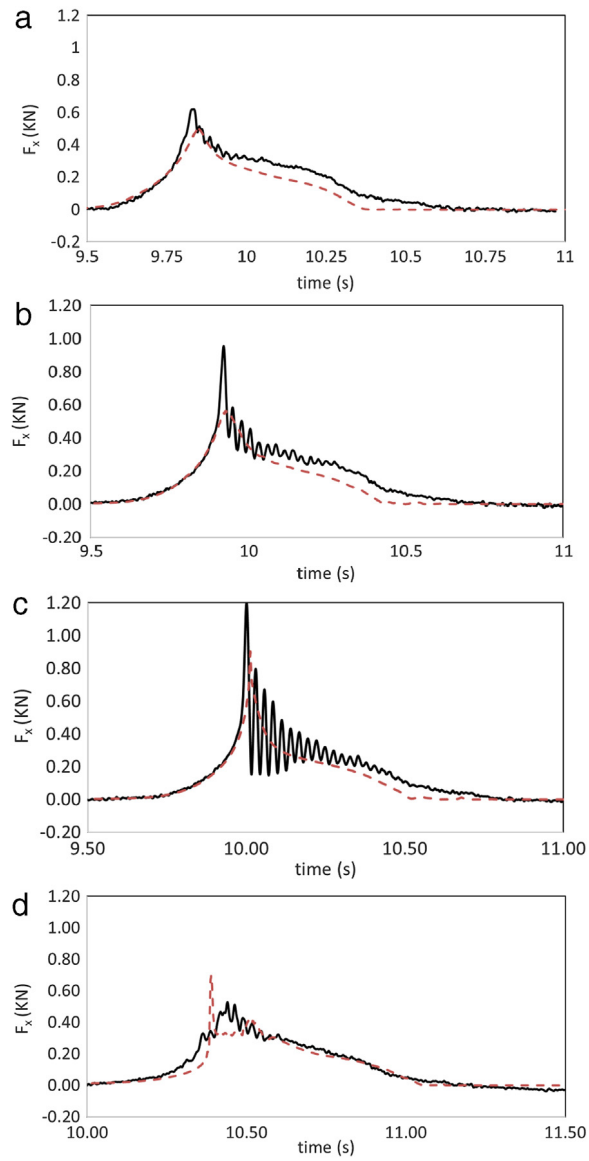


Fig. 11. Comparison of the horizontal force on the front hull section (a) slightly-breaking (b) flip-through (c) large air pocket (d) broken wave (— Phy. Exp., - - - OpenFOAM).

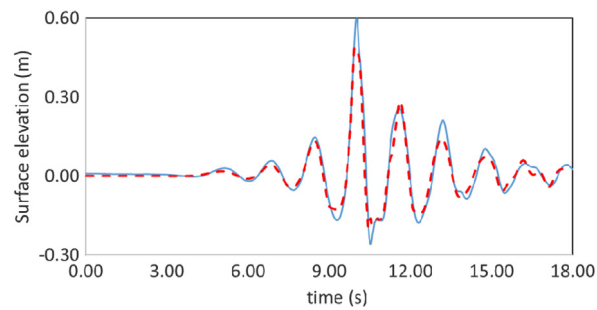


Fig. 12. Comparison of wave elevation at a position 0.015 m in front of the hull (— bottom mounted wall, - - - truncated hull).

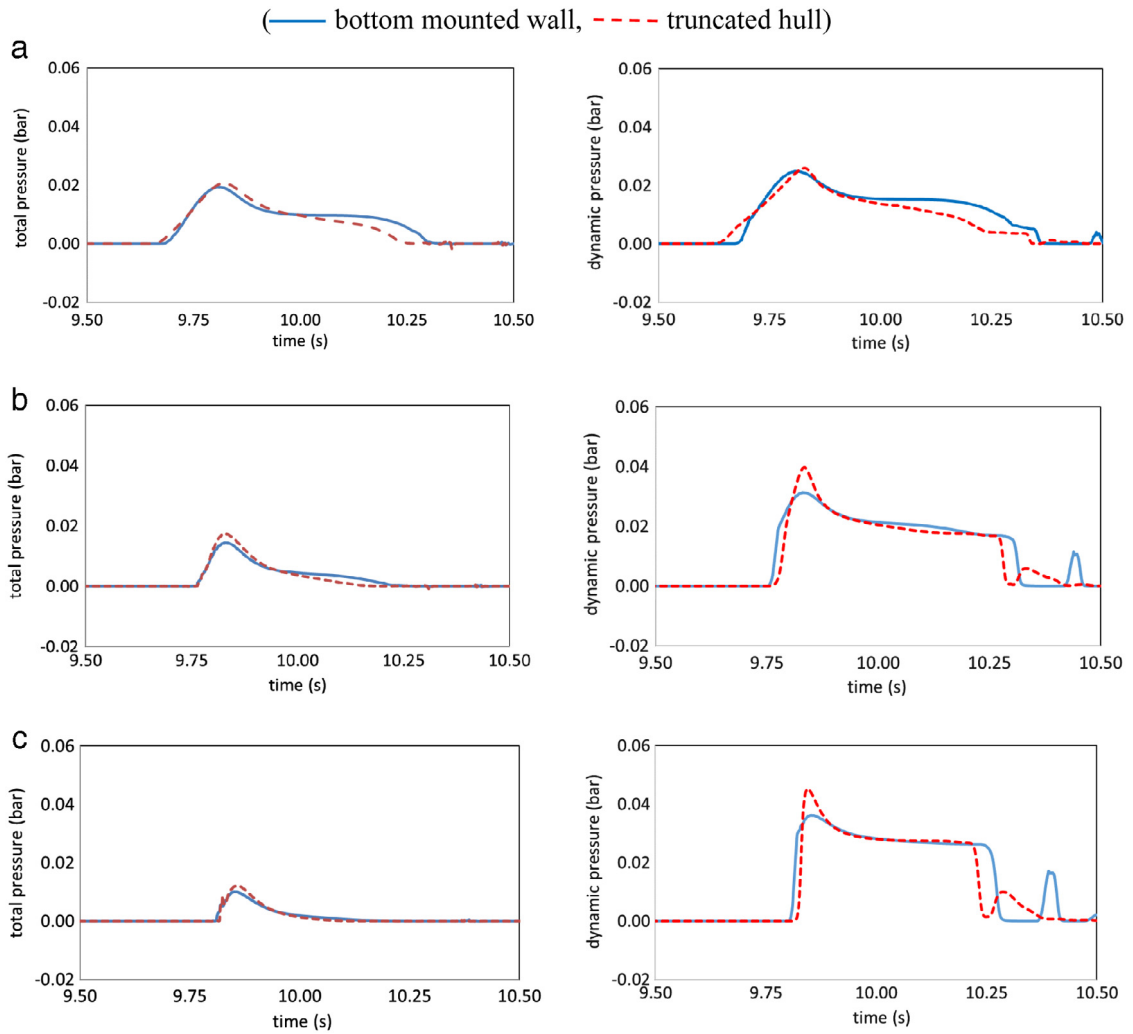


Fig. 13. Comparison of the total pressures in left hand side and the dynamic pressures in right hand side on the hull at (a) P6 (b) P9 (c) P11 (— bottom mounted wall, - - - truncated hull).

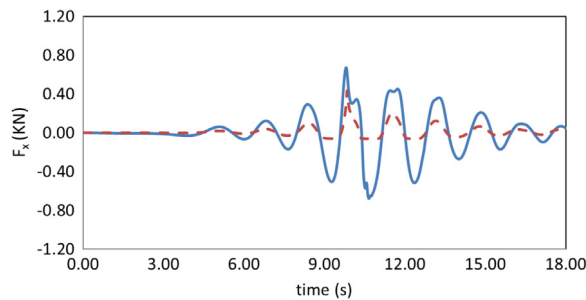


Fig. 14. Comparison of the horizontal force on the front hull section (— bottom mounted wall, - - - truncated hull).

hull is under the large air pocket wave impact. This may due to the air pockets, bubbles and turbulence produced under the impact, which spreads the high pressure region across the hull surface. It suggests that the large air pocket wave impact should be given greater consideration in coastal and ocean engineering design. Under the wave impacts with entrained air, high frequency oscillations observed in the pressure and force time history are due to a combination of the elastic response

of the hull and the oscillation of trapped air bubbles. Neither of these effects can be predicted by the numerical model used here, although the model is being extended to include these additional effects in ongoing work.

In summary, the results demonstrate that OpenFOAM is a suitable numerical tool for assessing wave impact on structures and the model presented here is well placed for extension to coastal and ocean engineering applications in a wide range of nonlinear wave conditions. Distinct characteristic wave impact types have been identified for the hull structure and different impact types are found to be responsible for different critical design parameters, such as maximum load and greatest wave run-up. Thus it is recommended that these cases are considered separately for design purposes and tests are carried out for a range of impact types.

Acknowledgements

This study is a part of the FROTH (Fundamentals and Reliability of Offshore sStructure Hydrodynamics) project supported by the Engineering and Physical Science Research Council (EPSRC Grant EP/J012866/1). The FROTH project is being led by Plymouth University and the collaborative partners include Oxford University, University of Bath, City University London and the Manchester Metropolitan University. The authors gratefully acknowledge the financial support provided by EPSRC and useful discussions with the project partners.

References

- Baldock, T.E., Swan, C., Taylor, P.H., 1996. A laboratory study of nonlinear surface waves on water. *Proc. R. Soc. Lond. A* 354, 650–675. <http://dx.doi.org/10.1098/rsta.1996.0022>.
- Bredmose, H., Bullock, G.N., Hogg, A.J., 2015. Violent breaking wave impacts. Part 3. Effects of scale and aeration. *J. Fluid Mech.* 765, 82–113.
- Bredmose, H., Hunt-Raby, A., Jayaratne, R., Bullock, G.N., 2010. The ideal flip-through impact: experimental and numerical investigation. *J. Engrg. Math.* 67 (1–2), 115–136. <http://dx.doi.org/10.1007/s10665-009-9354-3>.
- Brown, S., Greaves, D., Magar, V., Conley, D., 2015. Evaluation of turbulence closure models under spilling and plunging breakers in the surf zone, submitted for publication Coastal Engineering.
- Brown, S., Magar, V., Greaves, D., Conley, D., 2014. Numerical study of turbulent kinetic energy generation under breaking waves. In: 34th International Conference on Coastal Engineering, ICCE, Seoul, Korea, 15–20 June.
- Bullock, G.N., Obhrai, C., Peregrine, D.H., Bredmose, H., 2007. Violent breaking wave impacts. Part 1: Results from large-scale regular wave tests on vertical and sloping walls. *Coast. Eng.* 54, 602–617.
- Chan, E.S., 1994. Mechanics of deep water plunging-wave impacts on vertical structures. *Coast. Eng.* 22, 115–133.
- Chan, E.S., Melville, W.K., 1988. Deep-water plunging wave pressures on a vertical plane wall. *Proc. R. Soc. Lond. Ser. A* 417, 95–131.
- Colicchio, G., Colagrossi, A., Lugni, C., Brocchini, M., Faltinsen, O., 2007. Challenges on the numerical investigation of the flip-through. In: Proceedings of the 9th International Conference on Numerical Ship Hydrodynamics, pp. 380–394.
- Cooker, M.J., Peregrine, D.H., 1990. Computation of violent wave motion due to waves breaking against a wall. In: Proceedings of the 22nd International Conference on Coastal Engineering, ASCE, Delft, pp. 164–176.
- Dold, J.W., 1992. An efficient surface-integral algorithm applied to unsteady gravity-waves. *J. Comput. Phys.* 103, 90–115.
- Goda, Y., 2000. *RandOm Seas and Design of Maritime Structures*. World Scientific.
- Guilcher, P.M., Couty, N., Brosset, L., Le Touzé, D., 2013. Simulations of breaking wave impacts on a rigid wall at two different scales with a two-phase fluid compressible SPH model. *Int. J. Offshore Polar Eng.* 23 (04), 241–253.
- Guilcher, P.M., Oger, G., Jacquin, E., Brosset, L., Grenier, N., Le Touzé, D., 2014. Simulation of liquid impacts with a two-phase parallel SPH model. *Int. J. Offshore Polar Eng.* 24 (01), 11–20.
- Hattori, M., Arami, A., Yui, T., 1994. Wave impact pressure on vertical walls under breaking waves of various types. *Coastal Eng.* 22 (1–2), 79–114.
- Hu, Z.Z., Causon, D.M., Mingham, C.M., Qian, L., 2009. Numerical wave tank study of a wave energy converter in heave. In: Proceedings 19th International Society of Offshore and Polar Engineers (ISOPE) conference, Osaka, Japan, pp. 383–388.
- Hu, Z.Z., Causon, D.M., Mingham, C.G., Qian, L., 2010. Numerical simulation of nonlinear wave interactions with a wave energy converter. In: Proceedings of 20th International Society of Offshore and Polar Engineers (ISOPE) conference, Beijing, China, pp. 871–876 in Wave Energy Issue.
- Hu, Z.Z., Causon, D.M., Mingham, C.G., Qian, L., 2013a. The Cartesian cut cell free surface capturing method for 3D water impact problems. *Int. J. Numer. Methods Fluids* 71 (10), 1238–1259.
- Hu, Z.Z., Causon, D.M., Mingham, C.G., Qian, L., 2013b. Numerical simulation of water impact on a wave energy converter in free fall motion. *Open J. Fluid Dyn.* 3, 109–115.
- Hu, Z.Z., Greaves, D., Raby, A., 2014. Simulation of extreme free surface waves using OpenFoam. In: 5th Conference on the application of physical modelling to port and coastal protection, Varna, Bulgaria, Vol. 2, pp. 243–252.
- Hu, Z.Z., Greaves, D., Raby, A., 2016. Numerical Wave Tank Study of Extreme Waves and Wave-Structure Interaction Using OpenFoam®. *Ocean Eng.* 126, 329–342. <http://dx.doi.org/10.1016/j.oceaneng.2016.09.017>.
- Hull, P., Müller, G., 2002. An investigation of breaker heights, shapes and pressures. *Ocean Eng.* 29, 59–79.
- Jasak, H., 1996. Error analysis and estimation for the finite volume method with applications to fluid flows, Ph.D. thesis, Imperial College of Science, Technology and Medicine.
- Khayyer, A., Gotoh, H., 2009. Modified moving particle semi-implicit methods for the prediction of 2D wave impact pressure. *Coastal Eng.* 56, 419–440.
- Kimmoun, O., Malenica, S., Scolan, Y.M., 2009. Fluid structure interactions occurring at a flexible vertical wall impacted by a breaking wave. In: Proceedings 19th International Society of Offshore and Polar Engineers (ISOPE) conference, Osaka, Japan, pp. 308–315.
- Kimmoun, O., Ratouis, A., Brosset, L., 2010. Sloshing and scaling: experimental study in a wave canal at two different scales. In: Proceedings 20th International Society of Offshore and Polar Engineers (ISOPE) conference, Beijing, China, pp. 33–43.
- Ma, Z.H., Causon, D.M., Qian, L., Mingham, C.G., Mai, T., Greaves, D., Raby, A., 2016. Pure and aerated water entry of a flat plate. *Phys. Fluids* 28, 016104. <http://dx.doi.org/10.1063/1.4940043>.
- Mai, T., Hu, Z.Z., Greaves, D., Raby, A., 2015. Investigation of Hydroelasticity: Wave Impact on a Truncated Vertical Wall. In: 25th International Society of Offshore and Polar Engineers (ISOPE) conference, Hawaii, USA, pp. 647–654, ISBN: 978-1-880653-89-0.
- Ning, D.Z., Teng, B., Eatock Taylor, R., Zang, J., 2008. Numerical simulation of nonlinear regular and focused waves in an infinite water-depth. *J. Ocean Eng.* 35 (8–9), 887–899.

- Ning, D.Z., Zang, J., Liu, S.X., Eatock Taylor, R.E., Teng, B., Taylor, P.H., 2009. free surface and wave kinematics for nonlinear focused wave groups. *Ocean Eng.* 36 (15–16), 1226–1243.
- Oumeraci, H., Kortenhaus, A., Allsop, W., de Groot, M., Crouch, R., Vrijling, H., Voortman, H., 2001. Probabilistic design tools for vertical breakwaters, chap. Hydraulic Aspects. Ch 2. A. A. Balkema, Lisse.
- Peregrine, D.H., Bredmose, H., Bullock, G.N., Hunt, A.C., Obhrai, C., 2006. Water wave impact on walls and the role of air. In: Proc. 30th Internat. Conf. on Coastal Engineering, San Diego.
- Peregrine, D.H., Bredmose, H., Bullock, G., Obhrai, C., Muller, G., Wolters, G., 2005. Water wave impact on walls and the role of air. In: Proc. 29th Int. Conf. Coastal Engineering, Vol. 4. World Scientific, Singapore, pp. 4005–4017.
- Roache, P.J., Ghia, K., White, F., 1986. Editorial policy statement on the control of numerical accuracy. *ASME J. Fluids Eng.* 108 (1), 2.
- Rodi, W., 1980. Turbulence Models and their Application in Hydraulics—a State-of-the-Art Review. IAHR Publication.
- Tanimoto, K., Takahashi, S., 1994. Design and construction of caisson breakwaters. *Japan. Exp. Coast. Eng.* 22, 57–77.
- Tromans, P.S., Anaturk, A.R., Hagemeyer, P., 1991. A new model for the kinematics of large ocean waves-application as a design wave. In: Proceedings 1st Inter, Offshore and Polar Engineering Conference, Edinburgh U.K.
- Westphalen, J., Greaves, D., Williams, C., Drake, K., Taylor, P., 2009. Numerical simulation of an oscillating cone at the water surface using computational fluid dynamics. In: Proceedings International Workshop on water waves and floating bodies, 19–22 April, Zeleznorsk, Russia.
- Westphalen, J., Greaves, D.M., Williams, C.J.K., Hunt-Raby, A.C., Zang, J., 2012. Focused waves and wave-structure interaction in a numerical wave tank. *Ocean Eng.* 45, 9–21.
- Westphalen, J., Greaves, D.M., Williams, C.K., Zang, J., Taylor, P.H., 2008. Numerical simulation of extreme free surface waves. In: Proceedings 18th International Society of Offshore and Polar Engineers (ISOPE) conference, Vancouver, Canada, July 6–11.
- Wood, D.J., Peregrine, D.H., Bruce, T., 2000. Study of wave impact against a wall with pressure impulse theory: Part 1, trapped air. *J. Waterw. Port Coast. Ocean Eng. ASCE* 126, 182–190.
- Zang, J., Gibson, R., Taylor, P.H., Eatock Taylor, R., Swan, C., 2006. Second order wave diffraction around a fixed ship - shaped body in unidirectional steep waves. *J. Offshore Mech. Arct. Eng.* 128, 10.